Journal of The Electrochemical Society

Water-Soluble Binders That Improve Electrochemical Sodium-Ion Storage Properties in a $NaTi_2(PO_4)_3$ Anode

Journal of The Electrochemical Society, 2023 **170** 050529

Water-Soluble Binders That Improve Electrochemical Sodium-Ion Storage Properties in a $NaTi_2(PO_4)_3$ Anode

Yan Zhang,[1,*,z] Alex Grant,[1] Aoife Carroll,[1] Umair Gulzar,[1,*] Matthew Ferguson,[1] Ahin Roy,[2,3] Valeria Nicolosi,[2,3] and Colm O'Dwyer[1,3,4,*,z]

[1]*School of Chemistry, and Tyndall National Institute, University College Cork, Cork, T12 YN60, Ireland*
[2]*School of Chemistry, Trinity College Dublin, Dublin 2, Ireland*
[3]*AMBER Research Center, Trinity College Dublin, Dublin 2, Ireland*
[4]*Environmental Research Institute, University College Cork, Cork T23 XE10, Ireland*

Water-soluble binders are demonstrated to provide significantly better capacity, cycle life stability and rate response for NASICON-type $NaTi_2(PO_4)_3$ Na-ion battery anodes during reversible sodiation compared to electrodes made using polyvinylidene difluoride-containing slurries. The role of carboxymethyl cellulose (CMC) binders on the physical structure and chemical interfacial reactions with sodium-poor $NaTi_2(PO_4)_3$ are uncovered using electron microscopy and spectroscopy data and we show that a more stable NASICON $NaTi_2(PO_4)_3$ structure is found from the desodiation process from compensation of sodium deficiencies in the $NaTi_2(PO_4)_3$ by extra sodium from the CMC binder. When the binder comprises CMC and a styrene butadiene rubber (SBR) additive, the electrode delivers significantly better voltammetric and galvanostatic electrochemical response with a specific capacity of ~120 mAh g^{-1} with capacity retention of 90.5% for 500 cycles at 0.2 C (1 C = 133 mAh g^{-1}), and ~54 mAh g^{-1} at 20 C. The durability of the electrode during cycling and the stability of the redox processes ensures a higher capacity, longer cycle life electrode which is important for sustainable materials development for Na-ion technologies.
 [DOI: 10.1149/1945-7111/acd3b8]

Manuscript submitted March 27, 2023; revised manuscript received May 3, 2023. Published May 22, 2023.

While lithium ion batteries (LIBs) are the dominant battery technology in portable electronic devices and electrical vehicles, rechargeable batteries with increasing energy/power density (Wh Kg^{-1}, Wh l^{-1}), and lower costs (€/$/kWh) are being sought to fulfil the growing demands for next-generation sustainable energy storage and power systems.[1–8] Sodium is more abundant and cheaper (0.0017 wt% and 2.3 wt% for Li and Na, respectively) and as it has some similar physical-chemical properties to that of lithium ions, sodium ion batteries (SIBs) have captured widespread attention to be as a foundation/alternative for a next generation of batteries. Additionally, unlike lithium, sodium does not form an alloy with aluminum, so that the cost in SIBs further decreases by using cheaper aluminum current collectors (Al foil: $70 per 100 m, battery grade; Cu foil: $210 per 100 m, battery grade) for cathode/anode electrodes.

Today, considerable effort is devoted to SIBs development to find electrode material phases where the replacement of lithium by sodium in the crystal structure allows a high capacity, long life electrode.[9,10] For cathodes, Na-based layered transition-metal oxides have similar frameworks of MO_6 edge-sharing octahedra with $LiMO_2$ and are excellent candidates for high performance sodium storage. For example, layer structured $NaCoO_2$ and $NaFeO_2$ materials used as cathodes in SIBs show a specific capacity of 120 mAh g^{-1} and 80–100 mAh g^{-1}, respectively.[11–13] Additionally, Na-containing layer polyanionic compounds such as $NaFePO_4$ have been considered as potential cathodes in SIBs, and can deliver a reversible capacity of about 110 mAh g^{-1}.[14] They offer reasonable performance as practical cathodes, even though the cell voltage and specific capacity of layered Na-substituted metal oxide cathode materials in SIBs are less compared to analogue LIBs because of the larger cationic radius (Na:1.02; Li: 0.59 Å), higher molar mass (Na:23; Li: 7 g mol^{-1}) and more positive standard electrode potential (Na: −2.71 V vs NHE; Li: −3.05 V vs NHE) of the sodium ion. While graphitic carbon as an anode in commercial LIBs can exhibit a capacity of 372 mAh g^{-1}, it delivers a sodium storage capacity of just 31 mAh g^{-1} and a low insertion potential (close to the deposition potential of metal Na), which cannot meet the requirement of SIBs applications and is a potential safety hazard.[15] As for Na-alloy types, they suffer from rapid capacity decay because of significant volume expansion during sodiation/desodiation processes, even though exhibiting reasonably high specific capacities. In this regard, the development of suitable anode materials with high energy storage capability, stable cycling stability, and better safety are still challenging and a key issue for SIBs deployment.

The polyanion-type $NaTi_2(PO_4)_3$ material, with a crystal structure of a Na-super-ionic conductor (NASICON), is considered a promising anode for sodium-ion batteries (SIBs).[16–18] Its "zero-stress" framework guarantees long-term cycling life, and high Na-ion conductivity ensures excellent rate performance. Since the first report by Demas et al.,[19] the two-phase mechanism including two additional reversibly sodium ions intercalating to form $Na_3Ti_2(PO_4)_3$ was put forward as the sodium storage process for $NaTi_2(PO_4)_3$ in SIBs. The theoretical capacity is 133 mAh g^{-1}, and its relatively safety and lower cost make it a candidate material for SIBs in future battery industries.[19–21]

At electrode fabrication level, the primary role played by the binder is to link the different electrochemically active and conductive particles together and to ensure the active material uniformly adheres to the current collector; uniformity and local aggregation are important for controlling the electrical and mechanical behavior of the electrode.[22] More effective methodologies including solvent and additive-driven improvement for preparing homogeneous slurries are vital for fabricating electrodes with high gravimetric and areal loading of active materials in bulk processing. Traditionally, poly (vinylidene fluoride) (PVDF), as a common commercial binder, possesses high chemical resistance, good thermal and electrochemical stability.[23] However, PVDF binders require N-methy-l-2-pyrrolidone (NMP) as a dispersion medium, which is an organic solvent with high toxicity, volatility and flammability. Additionally, PVDF binder swelling and its dissolution in nonaqueous liquid electrolytes cause problems of desquamation of electrode particles, which shortens cycle stability and exacerbates capacity fading.[24,25] As typical water-soluble binder, sodium carboxymethyl cellulose (CMC) is a linear polymeric derivative of cellulose with two special functional groups: one is the carboxylate anion with the β-linked glucopyranose residues that makes it soluble in water; the hydroxyl (–OH) groups give favorable adhesive strength and uniform active material dispersion in aqueous suspension.[26–28] CMC is viewed as

*Electrochemical Society Member.
[z]E-mail: yan.zhang@ucc.ie; c.odwyer@ucc.ie

being more environmentally friendly (water-based solvent), and with stable bonding properties, stronger adhesion etc., it has been shown to improve sodium storage performance compared to PVDF as the binder in SIBs. For example, CMC binders were reported to enhance cycling stability for Sb electrodes and sodium titanate electrodes as well as capacity retention compared to PVDF.[29,30]

However, CMC-based electrodes can suffer from inelasticity and brittleness in some formulations due to an overall lower Young's modulus and tensile strength.[31,32] In the last few years, the combination of CMC and styrene butadiene rubber (SBR) was developed to mitigate some of these issues for water-soluble binders in battery systems. As an elastomer, SBR strengthens binding force, adhesion, improves heat resistance, and overall electrode flexibility. Some studies have suggested that the limited oxidative stability of SBR in SBR/CMC-based electrodes is useful for forming a passivation layer at the electrode surface, further improving capacity retention compared to PVDF-based electrodes.[33–35] Another attraction is the lower cost of CMC (1–2 € kg^{-1}) and SBR (0.2–1 € kg^{-1}), compared with that of PVDF (15–18 € kg^{-1}),[36] in addition to safer and less polluting solvents. CMC-SBR composite binders have also been successfully applied to graphite-based negative electrodes by replacing the conventional PVDF binder in commercial LIBs.[37] Furthermore, the use of CMC-SBR has already been extended to Li-S systems.[38,39] According to the report from Huang et al., SBR-CMC mixture binders improves sulfur utilization and suppresses the agglomeration of Li_2S by serving as high adhesion agent as well as a strong dispersion medium. This was reported to allow homogeneous distribution of insulating sulfur and conductive carbon black (CB). The promoted capacity retention and stability for sulfur cathode using the SBR-CMC binder are achieved, showing a high specific capacity of 580 mA h g^{-1} after 60 cycles.[38] Given the reported benefits and basis for stability and improvement in performance and electrode processing from CMC and CMC-SBR binders, we decided to explore how the PVDF, CMC and CMC-SBR binders function in Na-ion batteries. In particular, our work here examines the binders influence on the two-phase sodium storage mechanism of $NaTi_2(PO_4)_3$ anodes in SIBs and compares the relative behavior of these binders for the first time.

Here, we synthesized quasi-cubic architecture $NaTi_2(PO_4)_3$ (NTP) materials using the hydrothermal method and explored the effects of traditional PVDF binder, water-soluble CMC binder, and CMC binder with SBR additive, on the structural stability and sodium storage performance of NASICON $NaTi_2(PO_4)_3$ anodes. In comparison to PVDF, we show that the water-soluble binder improves the electrochemical properties and stability of the slurry on the current collector. The structural stability and phase integrity of the $NaTi_2(PO_4)_3$ material with water-soluble CMC binder leads to improved electrochemical reversibility, capacity and durability compared to equivalent electrodes fabricated with PVDF as binder. We show that the use of SBR additive enhances the Super-P-$NaTi_2(PO_4)_3$ slurry adhesion to the current collector, enabling continuous fast ion/electron transfer particularly for faster charge-discharge rates.

Experimental

Materials preparation.— *Preparation of $NaTi_2(PO_4)_3$.*—In a typical synthesis, 1.2 g sodium acetate (CH_3COONa) was dissolved in a mixed solvent of isopropyl alcohol ($CH_3CH_2CH_2OH$), 85 wt% phosphoric acid and acetic acid (CH_3COOH). The solution was stirred constantly for 24 h. Secondly, Titanium(IV) isopropoxide ($C_{12}H_{28}O_4Ti$, TTIP) was added dropwise into the above solution and further stirred for another 12 h. All liquid precursors are used with a volume ratio of 25:1:1:1. Subsequently, the as-formed white suspension was transferred into 100 ml Teflon-lined stainless-steel autoclaves and kept in an oven for 12 h at 200 °C. After cooling down to room temperature, the white precipitates in the hydrothermal autoclaves collected by centrifugation and washed three times with absolute ethanol and deionized water.

Materials characterization.—Scanning electron microscopy (SEM, Zeiss Supra 40) and transmission electron microscopy (TEM, JEOL JEM-2100F, 200 kV) were conducted to investigate the morphologies and structure of the materials. The X-ray diffraction (XRD, a Philips Xpert PW3719, diffractometer with Cu Kα radiation ($\lambda = 1.542$ Å)) was used to analyze the crystalline structure in the composite. High angle annular dark field TEM measurements and electron energy loss spectroscopic (EELS) mapping of electrode materials were acquired using a FEI Titan 80 FEG S/TEM (80–300 kV). The Fourier transform infrared (FT-IR) spectral measurements were carried out on a FT-IR spectrometer (Perkin-Elmer BX-2, U.S.A) at room temperature in the wave number range of 4000–500 cm^{-1}. Raman scattering was acquired using a Renishaw InVia Raman Spectrometer using a 30 mW Ar-ion laser under 532 nm excitation. The beam was focused onto the samples using a 50× objective lens and spectra were collected using a RenCam CCD camera.

Electrochemical measurements.—The electrochemical performances of obtained NTP products were evaluated by assembling El-Cell cells (ECC1–01–0012-A/L, 18 mm diameter, 0.65 mm thickness) as half-cells. All electrochemical tests were conducted on a multichannel BioLogic VSP Potentiostat/Galvanostat. Electrodes were examined using cyclic voltammetry, constant current (galvanostatic) potentiometry, and potential steps. The details of potentials, applied currents, scan rates or voltage ranges are provided in the captions to each relevant figure. The electrodes were prepared via a traditional slurry coating procedure. The slurries were obtained by mixing the NTP active material, conductive carbon (Super-P) and binders in the mass ratio of 8:1:1. The slurry mixtures were homogenized in N-methy-2-pyrrolidinone (NMP) for polyvinylidene fluoride (PVDF) binder or deionized water for sodium carboxymethyl cellulose (CMC) binders and CMC with styrene-butadiene-rubber (SBR) binders. The obtained electrodes were first dried in a vacuum oven at 80 °C for 12 h. After drying, electrodes were punched into discs with a diameter of 15 mm and used as the anode for SIBs. The EI-Cell cells assembled in an argon-filled glovebox (Inert I-Lab, H_2O/O_2 content <1 ppm). Lithium metal was used as the counter electrode, glass fiber was used as the separator, and the electrolyte consisted of 1 M sodium perchlorate ($NaClO_4$, Alfa Aesar, ⩾99%) in propylene carbonate (PC, $C_4H_6O_3$, Sigma-Aldrich, 99.7%) with 5% fluoroethylene carbonate ($C_3H_3FO_3$, Alfa Aesar, ⩾99%) additive.

Results and Discussion

Morphology and structure of the $NaTi_2(PO_4)_3$ and binder slurries.—The crystal structure and phase formation of the composites are confirmed by XRD and Raman spectrums. As shown in Fig. 1a, the diffraction reflections in the XRD patterns match well with NASICON-structured $NaTi_2(PO_4)_3$ (JCPDS file No.00-033-1296). The typical surface characteristics of as-prepared NTP powders were also recorded using Raman scattering spectra in the range of 200−1600 cm^{-1} (Fig. 1b). The peaks between 400 and 1200 cm^{-1} are assigned to the symmetric/antisymmetric bending models and stretching vibrations of $(PO_4)^{3-}$ anion (peaks at 1098 and 1013 cm^{-1}: $\nu 1$ symmetric stretching mode; peaks at 975 and 996 cm^{-1}: $\nu 3$ antisymmetric stretching mode; weak peaks in the 500–900 cm^{-1}: $\nu 3$ antisymmetric stretching mode; peak at 445 cm^{-1}: $\nu 2$ symmetric stretching mode). A series of bands below 400 cm^{-1} is attributed to external modes of the PO_4 tetrahedra.[21,40]

The residual functional groups on the NTP electrodes with each of the different binders are confirmed by the FTIR spectra in Figs. 1c and 1d. The NTP electrodes prepared with PVDF show similar spectral features from PVDF at 1400, 1186 and 878 cm^{-1}, and are dominated by strong signals originating from NTP at 1226, 960, 640, 569 cm^{-1}.[41,42] The NTP electrodes containing CMC or CMC–SBR display characteristic groups of vibrational modes from NTP at similar wavenumbers, and display typical signals at 1594, 1413 and

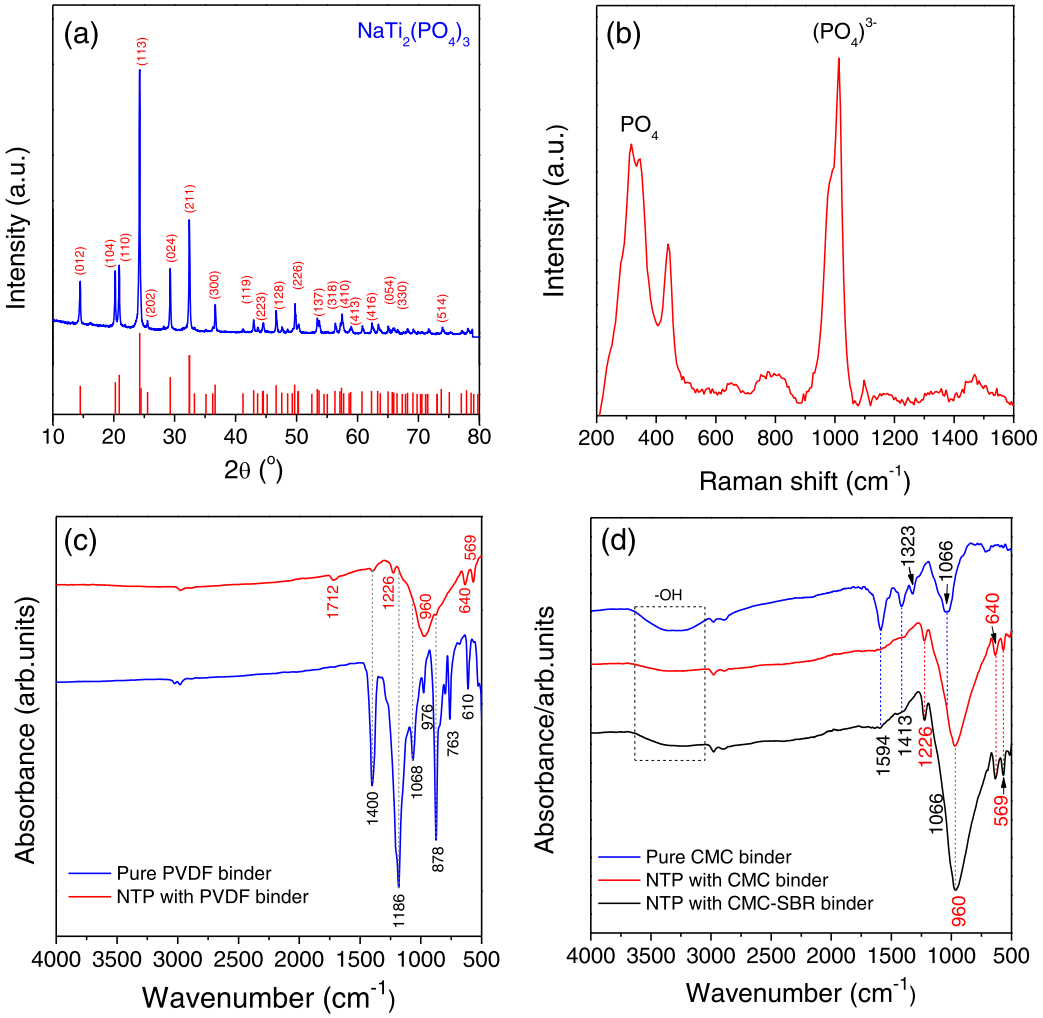

Figure 1. (a) X–ray diffraction pattern of the $NaTi_2(PO_4)_3$ anode material following hydrothermal synthesis. The reflections are indexed to the reference JCPDS file No. 00–033–1296. (b) Raman scattering spectra for NTP nanoparticulate material acquired under 532 nm excitation. (c) FTIR spectra of pure PVDF binder and the NTP electrode slurried with PVDF binder. (d) FTIR spectra of pure CMC binder and of the NTP electrode mixed with CMC and CMC-SBR binders.

1066 cm^{-1} from the CMC binder.[41] For the typical characteristics of NTP in each of the three electrode formulations, the infrared band of 1226 cm^{-1} corresponds to the stretching vibration of PO_4 units; the bands at 1016 and 569 cm^{-1} are related to the P–O bonds from PO_4 tetrahedra, and the vibrations from Ti^{4+}–O^{2-} bonds of TiO_6 octahedra are evidence by the bands at 960 and 640 cm^{-1}.[21,42]

Compared to PVDF-containing electrode, the spectrum of NTP electrodes with water-soluble binders contain broad peaks between 3000–3500 cm^{-1} in CMC electrodes from hydrogen bonded O–H stretching vibrations, and the two absorption peaks at 1413 and 1594 cm^{-1} are attributed to the –COOH group.[43–45] The presence of the large polar functional groups from the CMC binder provides sufficient adsorption sites to bind with NTP nanoparticles. Strong hydrogen bonding between CMC and anode materials has been previously demonstrated to be a vital factor that determines the cycling performance of the electrode.[46,47]

The structural, morphological properties and chemical composition of as-synthesized NTP nanoparticles are further confirmed by SEM and TEM analysis. As shown in Figs. 2a and 2b, the nanoparticles are relatively uniform and have average dimensions of 20–30 nm. TEM images (Fig. 2c) further demonstrate the nanoparticles appeared quasi-cubic in shape. These particles are typically ~20 nm in size. Dark field HAADF-STEM images (Figs. 2d–2e) show the cubic morphology in projection of the NTP crystals. Detailed elemental and oxidation state analysis was conducted using electron energy loss spectroscopic mapping. The EELS maps in Figs. 2f–2h confirm the co-existence of Ti, O (the orange box in Fig. 2d, and Na (the orange box in Fig. 2e). The EELS spectrum for the Ti $L_{2,3}$ edge is consistent with Ti^{4+} bonded to O.

Electrochemical response of $NaTi_2(PO_4)_3$ with various binders: Rate response.—In processing the $NaTi_2(PO_4)_3$ electrode, the binder solutions were uniformly diluted to translucency by stirring the PVDF powders with NMP, and the CMC powder with DI water. Second, the $NaTi_2(PO_4)_3$ active powders and Super-P were added to the binder solutions in the same proportions of mass to obtain the electrode slurry. As shown in the photograph in Fig. 3a, the electrodes have a similar appearance. Typical of the PVDF–containing slurry, the electrode shows a flaky outer edge from being slightly more fragile and lower adhesion to the current collector.

Typically, the rate performance is a key evaluation factor for benchmarking electrodes in batteries for practical applications. We characterized each of the three slurries using two methods. Standard charge–discharge behavior (galvanostatic) was used in cells ranging over two orders of magnitude from 0.2 C to 20 C. Secondly, we employed the chronoamperometric (CA) response method, which uses a constant potential method to examine the rate behavior of an electrode spanning many orders of magnitude in rate in a fraction of the time compared to galvanostatic cycling methods. Readers are referred to several papers that outline this approach.[48–52] Basically, a

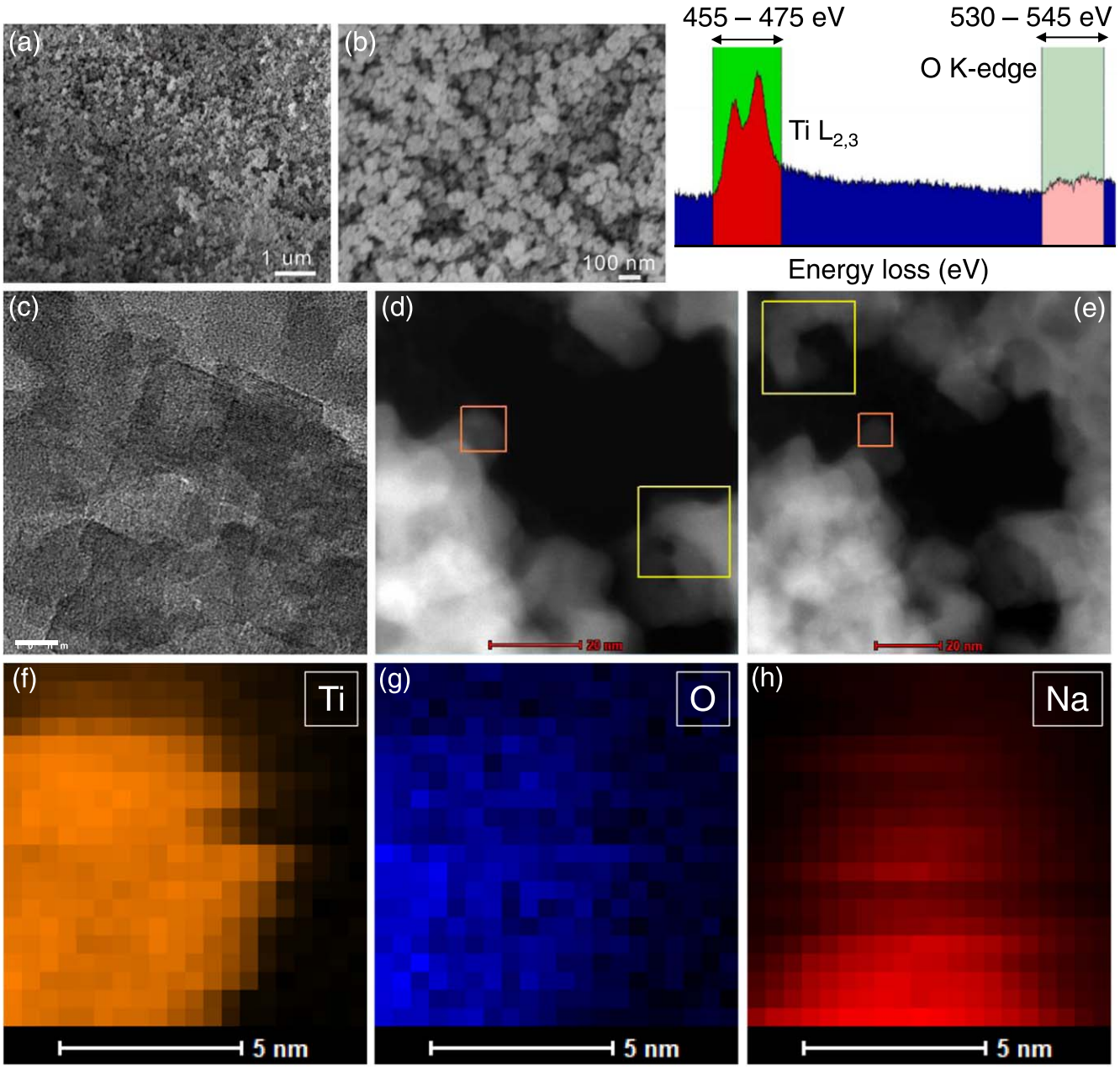

Figure 2. (a), (b) SEM images of the synthesized $NaTi_2(PO_4)_3$ materials showing the relatively uniform and dense agglomeration of the crystals of this phase. (c) The HRTEM image identified the cubic-like morphology of the crystals with many individual particles overlapped in projection. (d), (e) HAADF-STEM images of the same region at two different magnifications and EELS spectrum of the Ti $L_{2,3,}$ and O K edges. The bright regions are the $NaTi_2(PO_4)_3$ crystals (higher atomic number), the black regions are the chamber vacuum. (f), (g) EELS maps of Ti and O from the regions indicated by orange (smaller) box in (d), and similarly the Na map (h) from the orange boxed region in (e).

constant potential equivalent to the lower cut–off potential of the anode is applied and the current is measured vs time.[53,54] The current can be converted to charge and thus capacity vs rate data which accurately predicts that rate response of electrodes in just several minutes.

Figure 3b shows the specific capacity vs rate data for NTP electrodes with different binders. The fitted capacity-rate data were obtained on the basis of the following equation :$\frac{Q}{M} = Q_M[1 - (R\tau)^n(1 - e^{-(R\tau)^{-n}})]$.[48] Here, $\frac{Q}{M}$ represents the measured, rate–dependent specific capacity; Q_M is low–rate specific capacity, R is a fractional charge/discharge rate that is similar to the definition of C–rate but uses the maximum obtained capacity at the lowest rate instead of the theoretical capacity of the material, and τ is the characteristic time associated with charge/discharge. The exponent n is a constant and lies in the range 0–1. The equation describes the dependence of specific capacities $\left(\frac{Q}{M}\right)$ on current rate $\left(\frac{1}{R}\right)$. Thus, it provides a constant capacity at low rate. Whereas at high rate, the linear relationship ($n = 1.0$, $\frac{1}{R}$) between the specific capacity $\left(\frac{Q}{M}\right)$ and the current rate $\left(\frac{1}{R}\right)$ is presented as pure capacitive behavior such as in e.g., supercapacitors. The specific capacity $\left(\frac{Q}{M}\right)$ and the square root of the rate are linear proportional ($n = 0.5$, $\frac{1}{R^{1/2}}$) representing a diffusion limited battery material/system.[55,56]

The CA method is used here to evaluate the rate performance of electrode with different binders. As shown in Fig. 3b, a clear and significant improvement in rate performance can be seen in water-soluble binder electrodes. The specific capacities are higher when

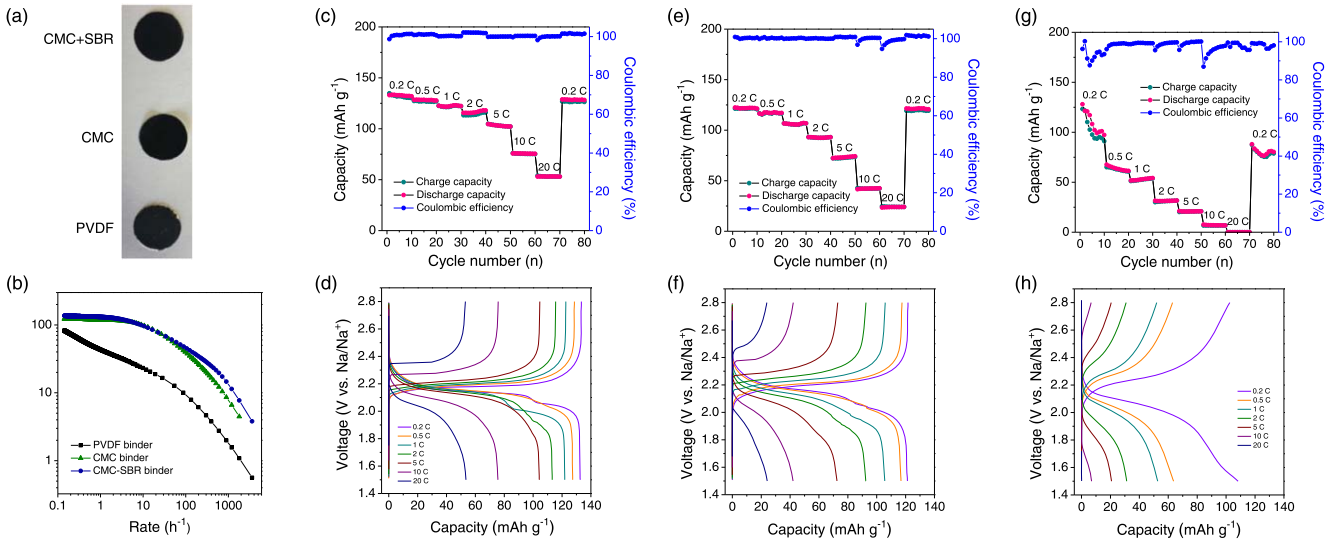

Figure 3. (a) Photos of NTP electrode slurries made with each of the three different binder mixtures. (b) Specific capacity vs rate data using chronoamperometry (CA) method for NTP anodes with CMC-SBR, CMC and PVDF binders. Here, the potential is stepped from OCV to the lower potential cut-off of 1.5 V and converted to Q/M vs rate (see main text). (c)–(h) Rate performance at various current densities corresponding to the two order of magnitude range 0.2 C–20 C and the corresponding charge-discharge profiles for (c), (d) NTP/CMC-SBR, (e), (f) NTP/CMC, (g), (h) NTP/PVDF electrodes.

using water-soluble binders than using organic PVDF binder at all investigated rates. It is notable that the specific capacities of approximately 80 mAh g^{-1} are exhibited at the extremely high rate of 100 C (1 C is defined as the current required to fully discharge/charge to 133 mA g^{-1} in 1 h) in water-soluble binder electrodes. Unfortunately, for PVDF binder electrode, the capacity decreases quickly, the specific capacities are suppressed to ∼10 mAh g^{-1} when the current density is greater than 10 C. Additionally, it can be observed to the contribution of the addition of SBR on rate performance. There are no obvious improvements at low rates between 0.1 C and 2 C for CMC binder electrodes and CMC-SBR binder electrodes, where a stable capacity of ∼130 mAh g^{-1} is obtained. When the rate is more than 20 C, the electrodes using water-soluble binder with SBR exhibit superior rate capacity.

Conventional rate capability tests of NTP electrodes using each of the three binders were evaluated at different rates over ten successive cycles, as presented in Figs. 3c, 3e and 3g. The corresponding charge-discharge curves for each electrode/binder, ranging from 0.2 C to 20 C, are shown in Figs. 3d, 3f and 3h. For NTP electrode using CMC-SBR binders, the specific capacity scales from 132.9 mAh g^{-1} at 0.2 C to, 53.1 mAh g^{-1} at 20 C. An electrode using water-soluble CMC binder without any SBR delivers a similar specific capacity decay at lower rates (121.3 mAh g^{-1} at 0.2 C to 72.5 mAh g^{-1} at 5 C). However, when charged/discharged at high rates of 10 and 20 C, a much lower specific capacities of ∼42.1 mAh g^{-1} and 24.1 mAh g^{-1} are found, close to the half of the values from the NTP electrode with SBR additive; the additive improves high-rate performance. In comparison, the specific capacity for NTP electrodes using PVDF binder diminished drastically from 108.3 mAh g^{-1} (0.2 C) to 20.7 mAh g^{-1} (5 C). The capacity fades to less than 10 mAh g^{-1} at high rates of 10 C and 20 C. Because the capacity fully recoveries when the rate is returned to 0.2 C confirms that the suppressed high-rate capacity is caused by the intrinsically higher electrical resistance at higher specific currents. CMC-SBR electrodes behave more stably at a higher rate. These changes agree with the potential step CA data in Fig. 3b. Both electrodes using water-soluble binders exhibit a symmetrical voltage plateau in their charge-discharge response at ∼2.1 V vs Na^+/Na due to the reversible redox pair of Ti^{4+}/Ti^{3+}.[19,20] Even at a rate of 20 C, these plateaus are still observed in NTP electrodes using the CMC-SBR binder. In comparison, the NTP electrodes with a PVDF binder show significant cell polarization and the fastest capacity fades higher specific currents. This data shows that the water-soluble CMC binder with SBR additive markedly improves the rate performance of NTP electrodes in SIBs, especially at the higher current rates. These improvements in rate performance are mainly ascribed to a more uniform electrode material (NTP and conductive carbon) additive dispersion in the slurry and adhesion, which presumably ensures good areal electrical interface between the current collector and the active material, compared to PVDF-containing electrodes.

Electrochemical response of $NaTi_2(PO_4)_3$ with various binders: Cycle life and efficiency.—The representative galvanostatic charge-discharge curves and cycle stability at the lower current density of 0.2 C are displayed in Fig. 4. In the first discharge-charge profiles, well-defined flat discharge plateaus at ∼1.95 V with a symmetric charge plateau at ∼2.25 V, are found in electrodes made with the CMC- and PVDF-based NTP slurries, and correspond to sodium ion insertion/extraction reactions of NTP coupled with Ti^{4+}/Ti^{3+} redox ($NaTi_2(PO_4)_3 + 2Na^+ + 2e^- \leftrightarrow Na_3Ti_2(PO_4)_3$). The primary charge storage reaction is consistent between all three electrodes. The differences in rate behaviour we showed earlier are not fundamentally caused by changes to this primary reaction. It is noted that all NTP electrodes show a slightly lower first discharge plateau just (< 2.0 V) compared to some previous reports where the plateau is found at ∼2.1 V. The slightly lower voltage in our case, by comparison, is assumed to be due to fewer sodium deficiencies or rich crystalline Ti-phases (TiP_2O_7) in our $NaTi_2(PO_4)_3$ electrodes.[57,58]

For NTP electrodes with water-soluble CMC binders, the similarly long stable charge plateaus (∼2.20 and 2.25 V) are observed in all subsequent cycles. The electrode shows a stable, reversible desodiation process. It is notable that the new charge plateau at ∼2.15 V is formed and the discharge-charge polarization seen in the first charge plateau disappears after the first 5 cycles. This indicates better reversibility during sodiation. A possible explanation might be that sodium ion availability from the CMC compensates the NTP material with a sodium deficiency to maintain a stable NTP structure during the discharging process. This hypothesis is further indicated by the sodiation/desodiation properties of the NTP electrodes using PVDF binders, which cannot provide additional sodium content. It is interesting to observe that there are two sloped discharge plateaus between 2.0–1.6 V in the first discharge process. The longer one is near 1.95–2.0 V, which is ascribed to sodium insertion into the structure of the $NaTi_2(PO_4)_3$ phase. The other shorter voltage plateau between 1.6 and 1.7 V might arise from the sodium storage contribution from a small amount of rich crystalline

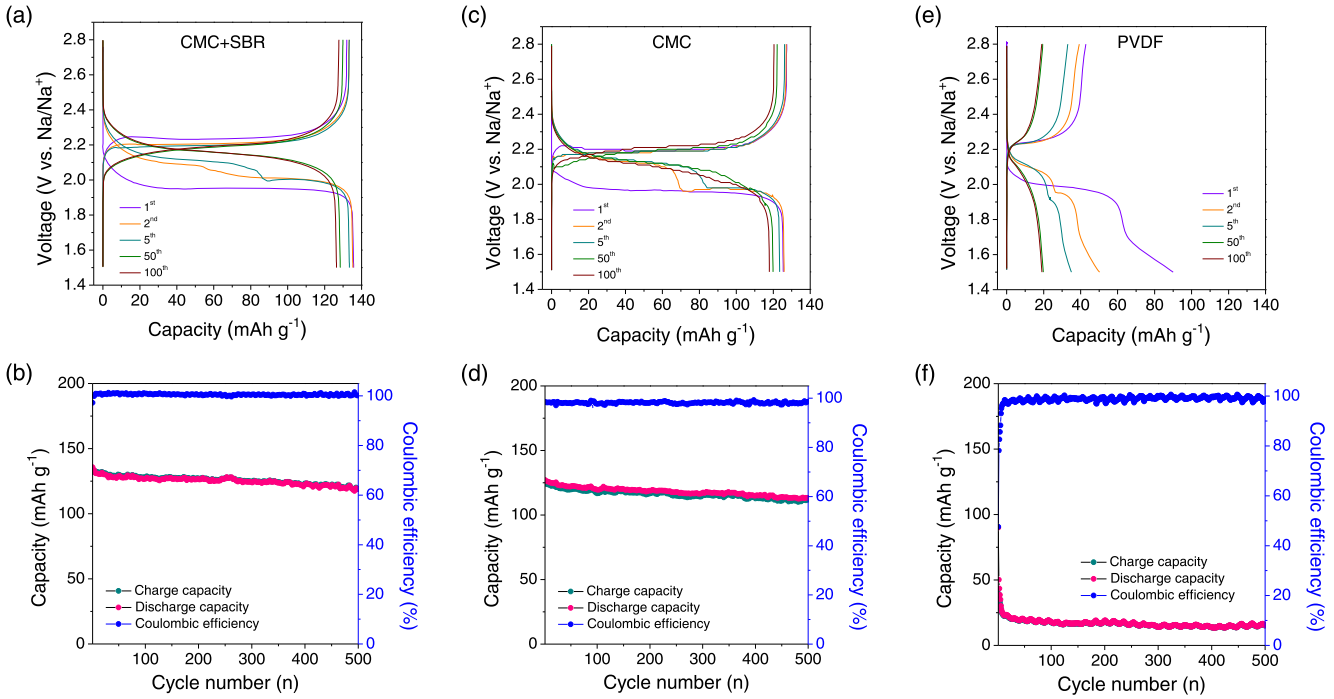

Figure 4. Galvanostatic charge-discharge curves and cycling stability tests for the $NaTi_2(PO_4)_3$ electrode slurries acquired at 0.2 C rate (capacity at 1 C = 133 mAh g^{-1}) over 500 cycles using (a), (b) CMC/SBR, (c), (d) CMC, and (e), (f) PVDF binders.

Ti-phases, which are not present in NTP electrodes with either CMC or CMC-SBR binders. $NaTi_2(PO_4)_3$ phases with a sodium deficiency that reacted with the CMC binder would form a stable chemically bonded C-$NaTi_2(PO_4)_3$ electrode when using water-soluble CMC binders. In addition, the discharge plateau near 1.95 V is not found to divide into two stages, and a larger voltage gap between charge and discharge plateaus (>180 mV) is present after the 2nd cycle. However, a very smaller discharge-charge voltage gap (CMC-SBR: 40 mV; CMC: 80 mV) in the electrode using the CMC is observed from the 2nd cycle and stays more or less invariant beyond 50 cycles. These results indicate the sodium-deficient $NaTi_2(PO_4)_3$ reacts with the sodium from CMC to form stable C-$NaTi_2(PO_4)_3$ electrodes and has a positive effect on reversible electrochemical reactions and faster kinetics for NTP electrodes using these binders.

The water-soluble binder-containing NTP electrodes yield higher initial discharge/charge specific capacities (CMC-SBR: 135.7/132.0 mAh g^{-1}; CMC: 127.2/125.4 mAh g^{-1}) and higher initial Coulombic efficiency (ICE) (CMC-SBR: 97.3%; CMC: 98.6%), whereas the PVDF binder NTP electrode provides a relatively low capacity (90/42.8 mAh g^{-1}) and a Coulombic efficiency level, ~50% lower overall. It indicates the initial Coulombic efficiencies for CMC/CMC-SBR electrode are much better than that of PVDF binders in the related literature (Table I). In these investigations we do find that the ICE for the first cycle is marginally lower that for CMC-only binder, but that is due to the oxidation of SBR during first charging sequence.[34,59]

The cycle-stability of NTP electrodes using water-soluble binder electrodes is also significantly improved compared to PVDF-binder-containing electrodes, as demonstrated in Figs. 4b, 4d and 4f. The CMC-SBR electrode responds with discharge/charge specific capacities as high as 119.7/119.5 mAh g^{-1} with a high Coulombic efficiency of 99.8% at the 500th cycle at 0.2 C rate. The CMC-containing electrodes exhibit a similarly high degree of sodium storage capacity as the CMC-SBR electrode, showing discharge/charge specific capacities of 127.2/125.4 mAh g^{-1} with a Coulombic efficiency of 98.5% at 500th cycle. The high-capacity retention for the NTP electrodes (CMC-SBR: 90.5%; CMC: 89.2%) indicates a very stable long-cycle performance when using water-soluble binders. By contrast, the NTP electrodes using PVDF binder undergo considerable capacity decay (~20% of the capacity of CMC-containing electrodes) because of the unstable sodium-deficient NTP phase, effects due to swelling of the PVDF polymer binder and the self-aggregation of NTP nanoparticles during cycling, issues that have been identified in previous report and that are mitigated effectively with CMC-based binders. These results demonstrate that higher specific capacities, better capacity retention and rate performance are possible using of CMC/CMC-SBR electrodes with $NaTi_2(PO_4)_3$ as the active material in Na-ion batteries when compared to previous reports in the Table I. The improvement is attributed to two main factors: (a) the extra sodium from CMC reacting with $NaTi_2(PO_4)_3$ unstable phases to form stable chemically-bonded C-$NaTi_2(PO_4)_3$ phases that improve NTP reversible utilization, and[2] more uniform dispersion of the NTP particles in the water-soluble binders and a stronger adhesive strength provided by the combination of water-soluble CMC binder and SBR additive, which favour higher ionic/electron conductivity, solvation and faster kinetics.

Voltammetric examination of $NaTi_2(PO_4)_3$ with various binders.—We used cyclic voltammetry to probe the electrochemical behaviour of NTP in each of the three binder-containing slurry mixtures. The voltammetric study removes constraints of galvanostatic polarization at fixed current (reaction rate), allowing a better comparison of the redox events in each electrode. Figure 5 presents the comparison of the typical cyclic voltammograms (CVs) of NTP electrodes with three different binders between 2.8 and 1.5 V. The tests were recorded at scan rates range from 0.1–1.0 mV s^{-1}. At a scan rate of 0.1 mV s^{-1}, all curves show one pair of well-defined redox peaks in the first scan, and the initial reduction peaks between 1.8 and 1.95 V might be attributable to the low conductivity and sodium deficiencies of NTP electrodes. It is noted that, from the second voltammetric scan, the reduction peaks resolve into two peaks, one at ~1.9 V and another at ~2.08 V. We see an anodic shift in of the reduction peaks and reduced polarization of the NTP electrodes using CMC binders form the 2nd scan, mainly ascribed to increase the conductivity by the formation of C-$NaTi_2(PO_4)_3$ phase, consistent with previous reported NASICON-type materials.[20,21,64,65] The single oxidation peak remains consistent at ~2.3 V for all three

Table I. Comparison of NTP anodes in SIBs using different binders, focused on the initial coulombic efficiency, capacity retention and rate capacity.

Active materials	Binder material	Initial coulombic efficiency	Capacity retention	Rate capacity (mAh g^{-1})	References
Bare NTP quasi-cubic nanoparticles	CMC-SBR	97.3%	90.5% after 500 cycles	53.1 (20 C)	This work
	CMC	98.6%	89.2% after 500 cycles	24.1 (20 C)	
	PVDF	~47.6%	35.8% after 500 cycles	<10 (20 C)	
Bare NTP nanoparticles	PVDF	79%	58% after 200 cycles	Close to 0 (10 C)	20
Bare NTP nanoparticles	PVDF	/	~30% after 500 cycles	3 (2 C)	42
Bare NTP nanocubes	PVDF	/	72% after 1000 cycles	Close to 0 (10 C)	60
Bare NTP nanocubes	SA (Sodium Alginate)	/	85% after 1000 cycles	65–90 (10 C)	61
Bare NTP powder	PVDF	/	/	~5 (20 C)	62
Bare NTP/Ni foam	Binder free	/	68.4% after 500 cycles	20 (20 C)	63

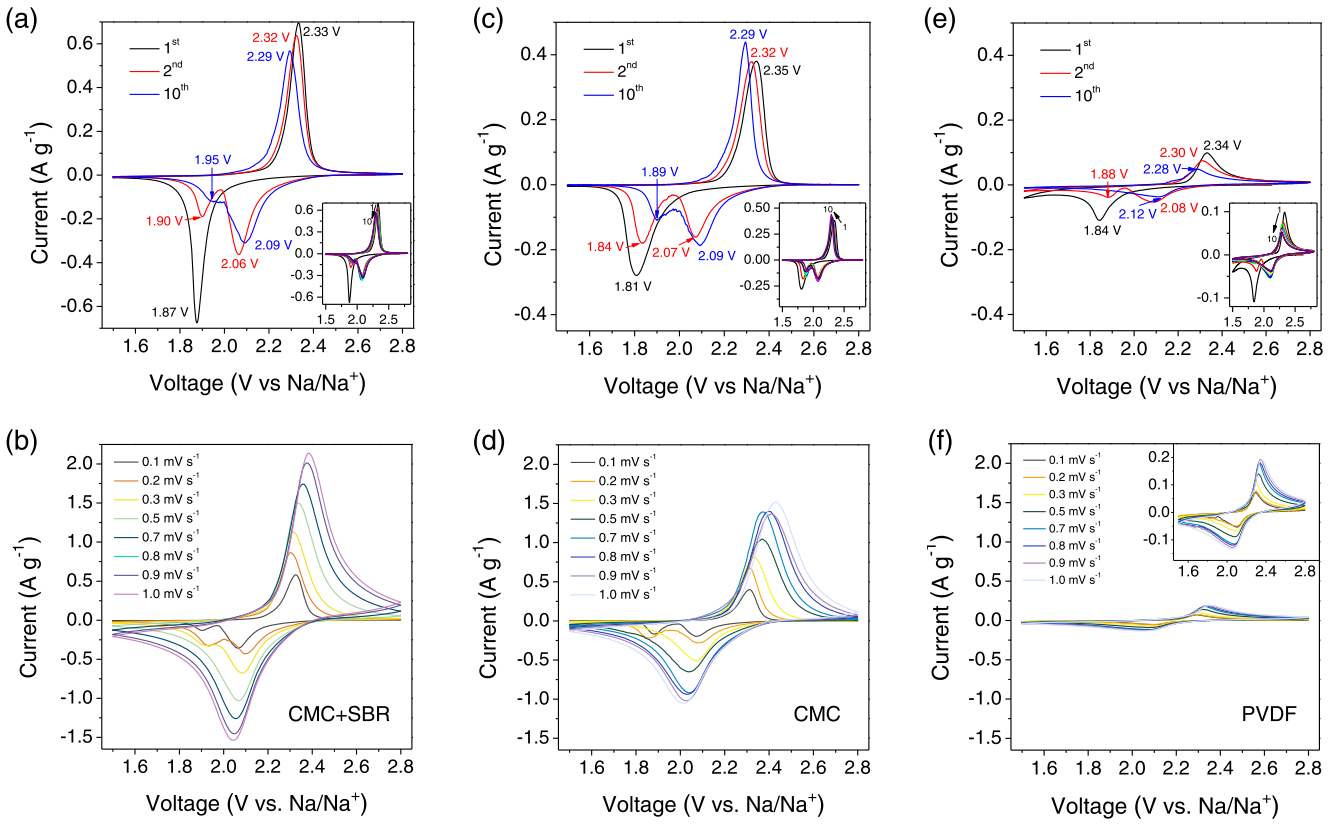

Figure 5. Cyclic voltammetry curves for NTP anodes slurried with each of the three binders. CV scans 1–10 are shown in each case at scan rates of 0.1 mV s^{-1} for NTP electrodes using (a) CMC-SBR, (b) CMC, and (c) PVDF binder. The CVs were carried out at scan rates in the range 0.1–10 mV s^{-1} between 1.5 and 2.8 V are also shown for (d) CMC-SBR, (e) CMC, and (f) PVDF binder.

electrode types, which indicates the oxidation production is always $NaTi_2(PO_4)_3 + 2Na^+ + 2e^- \leftrightarrow Na_3Ti_2(PO_4)_3$.[19] In addition, the reduction and oxidation peaks of the CMC-SBR/CMC electrodes are more defined and have a higher current than those from PVDF-based electrodes.

The initial first scan voltage difference ΔE between oxidation and reduction peaks for CMC-SBR electrodes (reduction: 1.87 V; oxidation: 2.33 V; ΔE: 0.46 V) is also smaller than found for the PVDF electrode (reduction: 1.84 V; oxidation: 2.34 V; ΔE: 0.50 V). This smaller voltage difference ΔE for the CMC-SBR/CMC electrodes also appears in the CV curves at high scan rate between 0.2 and 1.0 mV s^{-1}. Considering that the ΔE is determined by the potential polarization of the active material during the charge and discharge process, the lower ΔE and the sharper peak both demonstrate that the redox reactions in the NTP electrodes using CMC-soluble binders SBR cathode behave more likely as a Nernstian system. For CVs shown (Figs. 5b, 5d, 5f) with changes to scan rate (υ), we observed the classical increase in peak current (I_p) and shift in potential (E_p) with faster scan rates, and we find linear trends that follow the Randles-Sevcik relation I_p vs υ, and E_p vs ln(υ). While the examination confirms the likely diffusion-limited behavior of all electrodes, specific comparative interpretation is limited by a general lack of knowledge of the diffusion coefficient of the electroactive species in each case (so that the stoichiometry of the redox process can be compared), and confidence that the electrolyte and electroactive species remain unchanged.

We also examined the morphology of NTP electrodes made using water-soluble CMC binder and those made with the combination of CMC and the SBR additive, before and after cycling using scanning electron microscopy (SEM). The particle distribution of the pristine materials for CMC and CMC-SBR electrodes is homogeneous with no visible cracks (Figs. 6a and 6b). However, the PVDF systems show several agglomerates and disconnected areas from cracking. The uniform slurry morphology from the CMC and CMC-SBR binder is because of the carboxylate groups within the adsorbed layer of CMC that favors surface binding and strong adhesion to give a

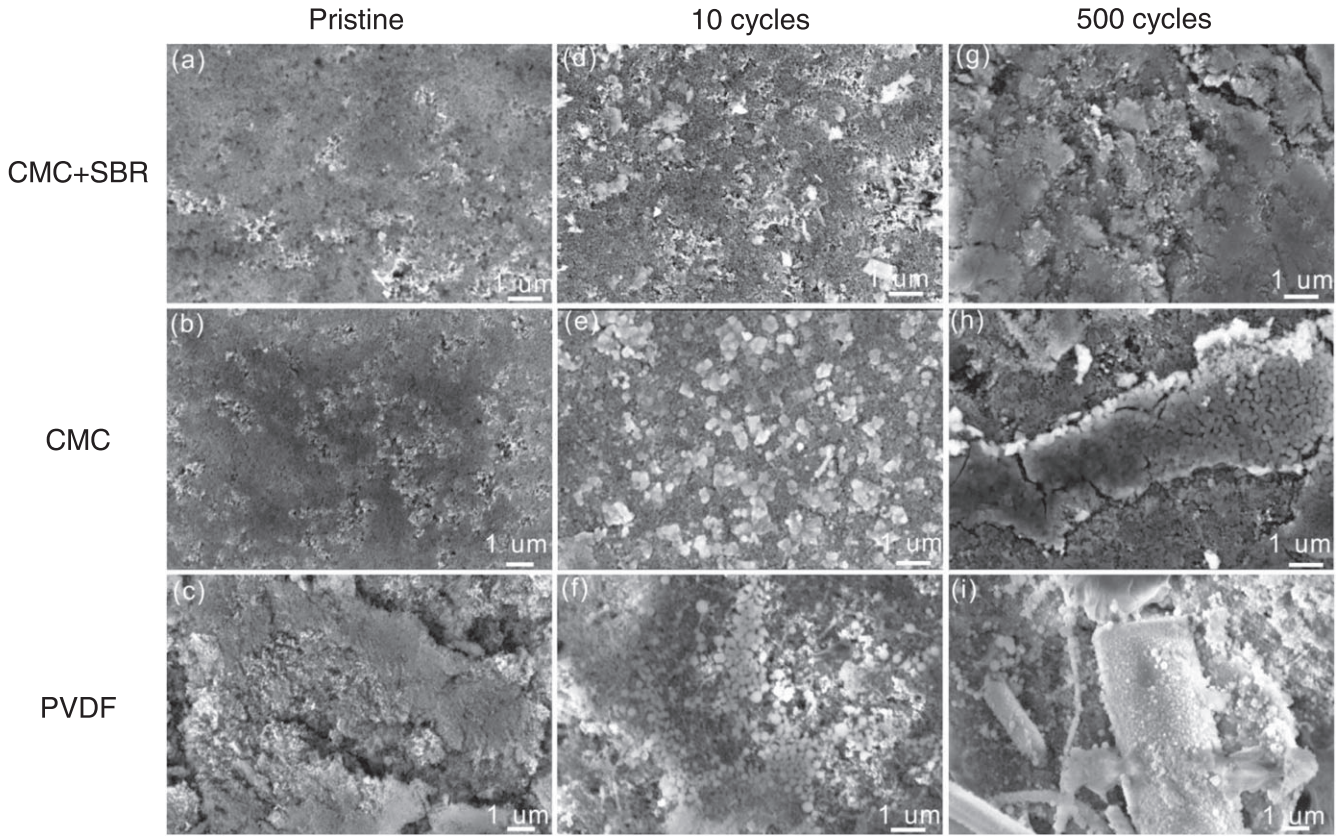

Figure 6. SEM images of the NTP electrode slurries on their current collectors in their pristine pre-cycled state using (a) CMC-SBR binder, (b) CMC binder, (c) PVDF binder. Images obtained after 10 cycles are also shown for electrodes using (d) CMC-SBR binder, (e) CMC binder, and (f) PVDF binder, and again after 500 cycles using (g) CMC-SBR binder, (h) CMC binder, and (i) PVDF binder.

material that accommodates expansion and plastic deformation.[66] As expected, the electrodes using the combination of CMC and SBR binders presented similar morphology and integrated structure after cycling for 10 and 500 cycles (Figs. 6d and 6g). This relative invariance of morphology and structure is in part a contributory factor in the excellent cycle stability for CMC-SBR electrodes. Small agglomerates and particle expansion does appear to happen in NTP electrodes using only CMC after extended cycling (Figs. 6e and 6h). However, numerous spheres of PVDF are found in NTP electrode using that binder (Figs. 6f and 6i) after cycling due to the swelling of PVDF and the structural reorganization during discharge and charge, which is likely to lead to the isolation of single carbon particles as well as formation of many interstices/disconnections inside the electrode. Undoubtedly, seriously deterioration in the electrode structure will lead to internal contact loss between the active materials, conductive and current collector, which gives rise to a large potential difference between charge and discharge plateaus, poor rate performance and cycling life, as we have shown. It can be concluded that the soluble CMC and CMC-SBR binders can provide a more effective electronically conductive network and a more stable interface structure than traditional PVDF binder. In particular, the addition of SBR in the water-soluble binder enables a stable chemically bonded C-$NaTi_2(PO_4)_3$ network structure to improve intra-particle electrical connectivity in an NTP electrodes that is not sodium-poor and behave with better stability over extended cycling and at all rates.

Conclusions

The electrochemical properties of $NaTi_2(PO_4)_3$ electrode slurries used in Na-ion batteries can be considerably improved by changing from a PVDF binder to a water-soluble CMC binder with SBR additive. This systematic investigated showed that electrodes applying water-soluble CMC binders show a significantly higher reversible capacity and initial coulombic efficiency, better high-rate performance and cycle stability, especially when combined with the SBR additive. The initial coulombic efficiencies of more than 97% are found when using the water-soluble CMC binder. The largest specific capacity of 120 mAh g^{-1} with the highest coulombic efficiency of 99.8% over 500 cycles at 0.2 C and a notable capacity of 53 mAh g^{-1} at high rate of 20 C are possible with the NTP electrode using CMC-SBR as co-binders. These improvement in the sodium storage behaviour and rate response stem from the formation of a C-$NaTi_2(PO_4)_3$ structure between the CMC binder and $NaTi_2(PO_4)_3$ active materials, as well as a stronger adhesive strength/flexibility of CMC and SBR binder to favour high ionic/electron conductive connection. In addition, for the electrodes using these water-soluble binders, we posit that the complex interfacial reactions between sodium deficient $NaTi_2(PO_4)_3$ and the additional sodium from CMC binder favours a more stable NASICON $NaTi_2(PO_4)_3$ structure during the electrode preparation and desodiation process. The evidence and data shown here indicate the sensitivity of behaviour and overall electrode performance in Na-ion batteries on the type of binder-active material pairing. The durability of the electrode during cycling and the stability of the redox processes ensures a higher capacity, longer cycle life electrode which is important for sustainable materials development for Na-ion technologies.

Acknowledgments

Y. Z. and C.O'D acknowledge support from the European Union's Horizon 2020 research and innovation program under grant agreement No 825114. C.O'D. acknowledges support from the Irish Research Council under an Advanced Laureate Award (IRCLA/19/118) and U.G. thanks IRC for support under the Government of

Ireland Postdoctoral Fellowship (GOIPD/2021/438). V. N. and A.R. wish to thank the support of the ERC CoG, 3D2DPrint (681544), SFI AMBER (12/RC/2278_P2) and SFI FFT R21/196.

ORCID

Umair Gulzar https://orcid.org/0000-0003-1429-5957
Valeria Nicolosi https://orcid.org/0000-0002-7637-4813
Colm O'Dwyer https://orcid.org/0000-0001-7429-015X

References

1. B. Dunn, H. Kamath, and J. M. Tarascon, *Science*, **334**, 928 (2011).
2. S.-W. Kim, D.-H. Seo, X. Ma, G. Ceder, and K. Kang, *Adv. Energy Mater.*, **2**, 710 (2012).
3. P. K. Nayak, L. Yang, W. Brehm, and P. Adelhelm, *Angew. Chem. Int. Ed.*, **57**, 102 (2018).
4. J. Xu, J. Liao, Y. Xu, J. Li, C. Zhu, J. Lin, and X. Zhou, *Journal of Energy Chemistry*, **68**, 284 (2022).
5. J. Xu, L. Duan, J. Liao, H. Tang, J. Lin, and X. Zhou, *Green Energy & Environment* (2022).
6. J. Sun, Y. Xu, Y. Lv, Q. Zhang, and X. Zhou, *CCS Chemistry*, **1**, 1 (2023).
7. L. Xu and C. V. Thompson, *J. Mater. Chem. A*, **8**, 21872 (2020).
8. H. Qian et al., *Electrochemical Energy Reviews*, **5**, 2 (2022).
9. Y. Liu, Y. Xu, Y. Han, Z. Zhang, J. Xu, Y. Du, J. Bao, and X. Zhou, *J. Power Sources*, **436**, 226860 (2019).
10. G. Xu, Q. Wang, Y. Su, M. Liu, Q. Li, and Y. Zhang, *Acta Phys.-Chim. Sin*, **38**, 2009073 (2022).
11. R. Berthelot, D. Carlier, and C. Delmas, *Nat. Mater.*, **10**, 74 (2011).
12. H. Yoshida, N. Yabuuchi, and S. Komaba, *Electrochem. Commun.*, **34**, 60 (2013).
13. K. Kubota, T. Asari, H. Yoshida, N. Yaabuuchi, H. Shiiba, M. Nakayama, and S. Komaba, *Adv. Funct. Mater.*, **26**, 6047 (2016).
14. P. Barpanda, S.-i Nishimura, and A. Yamada, *Adv. Energy Mater.*, **2**, 841 (2012).
15. M. M. Doeff, Y. Ma, S. J. Visco, and L. C. De Jonghe, *J. Electrochem. Soc.*, **140**, L169 (1993).
16. S. Chen, C. Wu, L. Shen, C. Zhu, Y. Huang, K. Xi, J. Maier, and Y. Yu, *Adv. Mater.*, **29**, 1700431 (2017).
17. M. Wu, B. Xu, Y. Zhang, S. Qi, W. Ni, J. Hu, and J. Ma, *Chem. Eng. J.*, **381**, 122558 (2020).
18. M. Wu, W. Ni, J. Hu, and J. Ma, *Nano-Micro Letters*, **11**, 44 (2019).
19. C. Delmas, F. Cherkaoui, A. Nadiri, and P. Hagenmuller, *Mater. Res. Bull.*, **22**, 631 (1987).
20. C. Wu, P. Kopold, Y.-L. Ding, P. A. van Aken, J. Maier, and Y. Yu, *ACS Nano*, **9**, 6610 (2015).
21. Y. Fang, L. Xiao, J. Qian, Y. Cao, X. Ai, Y. Huang, and H. Yang, *Adv. Energy Mater.*, **6**, 1502197 (2016).
22. J. Xing, S. Bliznakov, L. Bonville, M. Oljaca, and R. Maric, *Electrochemical Energy Reviews*, **5**, 14 (2022).
23. B. Ameduri and H. Sawada, *Fluorinated Polymers: Volume 2: Applications Volume 2: Applications* (Oxford, Royal Society of Chemistry)p. 1 (2016).
24. A. Magistris, P. Mustarelli, F. Parazzoli, E. Quartarone, P. Piaggio, and A. Bottino, *J. Power Sources*, **97-98**, 657 (2001).
25. P. Periasamy, K. Tatsumi, M. Shikano, T. Fujieda, Y. Saito, T. Sakai, M. Mizuhata, A. Kajinami, and S. Deki, *J. Power Sources*, **88**, 269 (2000).
26. M. Zarrabeitia, E. Castillo-Martínez, J. M. López Del Amo, A. Eguía-Barrio, M. A. Muñoz-Márquez, T. Rojo, and M. Casas-Cabanas, *J. Power Sources*, **324**, 378 (2016).
27. X. Ma, P. R. Chang, and J. Yu, *Carbohydr. Polym.*, **72**, 369 (2008).
28. N. Böckenfeld, S. S. Jeong, M. Winter, S. Passerini, and A. Balducci, *J. Power Sources*, **221**, 14 (2013).
29. M. Dahbi et al., *Electrochem. Commun.*, **44**, 66 (2014).
30. Y. Zhang, H. Hou, X. Yang, J. Chen, M. Jing, Z. Wu, X. Jia, and X. Ji, *J. Power Sources*, **305**, 200 (2016).
31. J. Chong, S. Xun, H. Zheng, X. Song, G. Liu, P. Ridgway, J. Q. Wang, and V. S. Battaglia, *J. Power Sources*, **196**, 7707 (2011).
32. J. Li, R. B. Lewis, and J. R. Dahn, *Electrochem. Solid-State Lett.*, **10**, A17 (2007).
33. H. Isozumi, T. Horiba, K. Kubota, K. Hida, T. Matsuyama, S. Yasuno, and S. Komaba, *J. Power Sources*, **468**, 228332 (2020).
34. N. Yabuuchi, Y. Kinoshita, K. Misaki, T. Matsuyama, and S. Komaba, *J. Electrochem. Soc.*, **162**, A538 (2015).
35. S. Hitomi, K. Kubota, T. Horiba, K. Hida, T. Matsuyama, H. Oji, S. Yasuno, and S. Komaba, *ChemElectroChem*, **6**, 5070 (2019).
36. F. M. Courtel, S. Niketic, D. Duguay, Y. Abu-Lebdeh, and I. J. Davidson, *J. Power Sources*, **196**, 2128 (2011).
37. J.-H. Lee, U. Paik, V. A. Hackley, and Y.-M. Choi, *J. Electrochem. Soc.*, **152**, A1763 (2005).
38. M. He, L.-X. Yuan, W.-X. Zhang, X.-L. Hu, and Y.-H. Huang, *J. Phys. Chem. C*, **115**, 15703 (2011).
39. M. J. Lacey, F. Jeschull, K. Edström, and D. Brandell, *J. Power Sources*, **264**, 8 (2014).
40. C. M. Burba and R. Frech, *Solid State Ionics*, **177**, 1489 (2006).
41. C. C. Nguyen, T. Yoon, D. M. Seo, P. Guduru, and B. L. Lucht, *ACS Appl. Mater. Interfaces*, **8**, 12211 (2016).
42. G. Pang, P. Nie, C. Yuan, L. Shen, X. Zhang, H. Li, and C. Zhang, *J. Mater. Chem. A*, **2**, 20659 (2014).
43. N. A. Choudhury, Y. Sahai, and R. G. Buchheit, *Electrochem. Commun.*, **13**, 1 (2011).
44. V. K. Mourya, N. Inamdara, and N. Ashutosh Tiwari, *Advanced Materials Letters*, **1**, 11 (2010).
45. L. Yue, L. Zhang, and H. Zhong, *J. Power Sources*, **247**, 327 (2014).
46. I. Kovalenko, B. Zdyrko, A. Magasinski, B. Hertzberg, Z. Milicev, R. Burtovyy, I. Luzinov, and G. Yushin, *Science*, **334**, 75 (2011).
47. J. S. Bridel, T. Azaïs, M. Morcrette, J. M. Tarascon, and D. Larcher, *Chem. Mater.*, **22**, 1229 (2010).
48. R. Tian, S.-H. Park, P. J. King, G. Cunningham, J. Coelho, V. Nicolosi, and J. N. Coleman, *Nat. Commun.*, **10**, 1933 (2019).
49. R. Tian, P. J. King, J. Coelho, S.-H. Park, D. V. Horvath, V. Nicolosi, C. O'Dwyer, and J. N. Coleman, *J. Power Sources*, **468**, 228220 (2020).
50. R. Tian, N. Alcala, S. J. K. O'Neill, D. V. Horvath, J. Coelho, A. J. Griffin, Y. Zhang, V. Nicolosi, C. O'Dwyer, and J. N. Coleman, *ACS Appl. Energy Mater.*, **3**, 2966 (2020).
51. C. Heubner, M. Schneider, and A. Michaelis, *Adv. Energy Mater.*, **10**, 1902523 (2020).
52. C. Heubner, M. Schneider, and A. Michaelis, *Adv. Energy Mater.*, **10**, 1902523 (2019).
53. C. Heubner, C. Lämmel, A. Nickol, T. Liebmann, M. Schneider, and A. Michaelis, *J. Power Sources*, **397**, 11 (2018).
54. U. Gulzar, A. Lonergan, V. Egorov, Y. Zhang, A. Grant, A. Carroll, and C. O'Dwyer, *J. Electrochem. Soc.*, **170**, 030503 (2023).
55. K. G. Gallagher et al., *J. Electrochem. Soc.*, **163**, A138 (2015).
56. C. Chen, Y. Wen, X. Hu, X. Ji, M. Yan, L. Mai, P. Hu, B. Shan, and Y. Huang, *Nat. Commun.*, **6**, 6929 (2015).
57. H. Hamad, J. Castelo-Quibén, S. Morales-Torres, F. Carrasco-Marín, A. F. Pérez-Cadenas, and F. J. Maldonado-Hódar, *Materials*, **11**, 1766 (2018).
58. Q. Zhang, C. Liao, T. Zhai, and H. Li, *Electrochim. Acta*, **196**, 470 (2016).
59. H. Isozumi, K. Kubota, R. Tatara, T. Horiba, K. Hida, T. Matsuyama, S. Yasuno, and S. Komaba, *ACS Appl. Energy Mater.*, **3**, 7978 (2020).
60. Y. Man, J. Sun, X. Zhao, L. Duan, Y. Fei, J. Bao, X. Mo, and X. Zhou, *J. Colloid Interface Sci.*, **635**, 417 (2023).
61. G. Yang, H. Song, M. Wu, and C. Wang, *J. Mater. Chem. A*, **3**, 18718 (2015).
62. Y. Niu, M. Xu, Y. Zhang, J. Han, Y. Wang, and C. M. Li, *RSC Adv.*, **6**, 45605 (2016).
63. Q. Hu, J. Liao, R. Xu, X. He, J. Wang, X. Ding, and C. Chen, *Energy Technology*, **7**, 1900386 (2019).
64. S. Li, Y. Dong, L. Xu, X. Xu, L. He, and L. Mai, *Adv. Mater.*, **26**, 3545 (2014).
65. M. Chen et al., *ACS Appl. Mater. Interfaces*, **12**, 50388 (2020).
66. B. Lestriez, S. Bahri, I. Sandu, L. Roué, and D. Guyomard, *Electrochem. Commun.*, **9**, 2801 (2007).